JOINT INSTITUTE FOR NUCLEAR RESEARCH

Flerov Laboratory of Nuclear Reactions

FINAL REPORT ON THE INTEREST PROGRAMME

Production and spectroscopic investigation of new neutron-rich isotopes near the neutron N=126 shell closure using the multinucleon transfer reactions

Supervisor:

Mr. Viacheslav Vedeneev

Student:

Solné Reyes Peña, Cuba

Higher Institute of Applied Sciences and Technologies

Participation period:

May 24 – July 2, Wave 4

Dubna, 2021

Abstract

The MASHA mass-separator designed for the production and mass identification of superheavy atoms using the solid ISOL method is described. The products of the nuclear reactions ^{40}Ar+^{148}Sm, ^{40}Ar+^{166}Er and ^{48}Ca+^{242}Pu performed at the MASHA setup were identified and studied by means of their alpha decay detection. The comparison of the decay energies obtained in the experiment with their respective literature values showed a relative deviation from the real ones of about 2%, for the majority of nuclides obtained. A graphical representation of the mass separation efficiency from the detection system is also presented.

Introduction

The production of superheavy nuclei and the searching of the Island of Stability is, nowadays, the most exciting and demanding task of Nuclear Physics. The study of the physical properties of superheavy elements (SHE), such as decay energy and modes, mass and half-lives has stimulated the design and construction of the Mass Analyser of Super Heavy Atoms (MASHA) at one of the beam outs of U-400M cyclotron based in Flerov Laboratory of Nuclear Reactions (FLNR) at Joint Institute for Nuclear Research (JINR), Dubna, Russia.

The unique potential of the mass analyser can be attributed to its capabilities of measuring the masses of synthesized superheavy element isotopes and, simultaneously, of detecting their α decays and (or) spontaneous fission [1].

Another possible application of the mass-separator MASHA would be related to studying the neutron-rich nuclei near the N=126 neutron shell. These nuclei are planned to be produced in the multi-nucleon transfer reactions with mass-to-charge ratio separation of the target-like fragments. The target+catcher system using Isotope Separation On-Line (ISOL) methodic, where the target material is solved in the catcher material will be used in this type of reactions. This has to be in favor of increasing the yield of fragments.

The reaction processes studied in this project were:

$$^{40}Ar + {}^{148}Sm \rightarrow {}^{188-xn}Hg + xn,$$

$$^{40}Ar + {}^{166}Er \rightarrow {}^{206-xn}Rn + xn,$$

$$^{48}Ca + {}^{242}Pu.$$

As can be seen, the first two reactions are complete fusion with neutron evaporation residues, while the last is a multinucleon transfer reaction, where

neutron-deficient mercury and radon isotopes were identified and studied through their α decay chains.

MASHA setup

The setup, the layout of which is shown in Fig. 1, consists of the target assembly with a hot catcher; an ion source based on the electron cyclotron resonance phenomena (ECR); a magneto-optical analyser (a mass spectrometer) composed of four dipole magnets (D_1, D_2, D_{3a}, and D_{3b}), three quadrupole lenses (Q_1, Q_2, Q_3), and two sextupole lenses (S_1, S_2); and a detection system located in the focal plane F of the spectrometer [1].

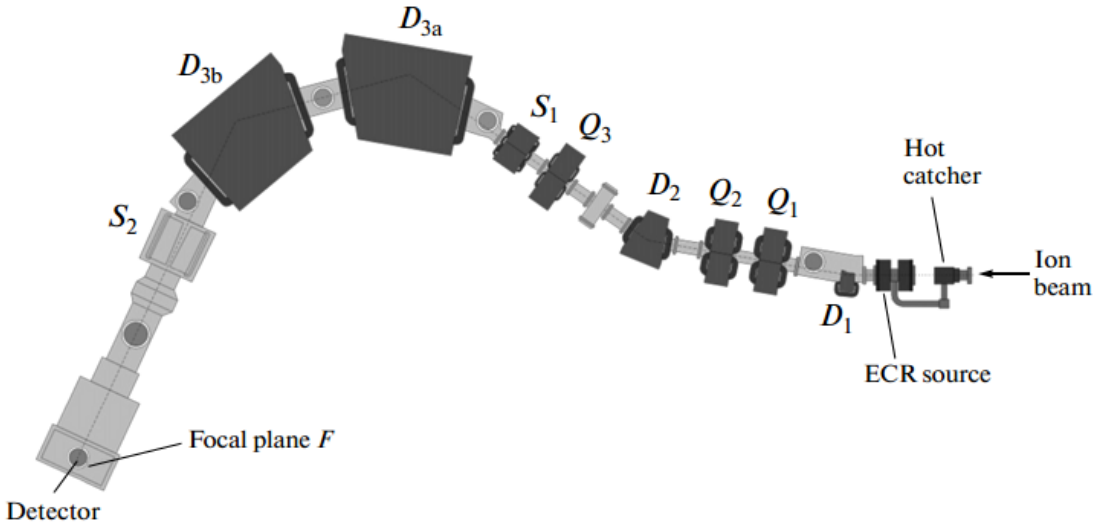

Fig. 1. Schematic diagram of the MASHA mass separator [1].

Target assembly and hot catcher

A schematic view of the target-catcher system is shown in Fig. 2. The target assembly uses the block of rotating targets, assembled into cassettes. The idea to use rotating target instead stationary is better efficiency and heat distribution. The disc rotated at the frequency of 25 Hz via Siemens electric engine. The division foil was changed to thin graphite foil in connection to its thermal reliability in comparison to titanium foil. Changings touched a heater also. Now it's fully modified and represents thermally expanded polygraphene structure heated directly by electric current. This removes the heating losses and irregularity of the heating [2]. The material of the catcher is flexible graphite, with a density of 1

g/cm^3, a thickness of 0.6 mm and shaped as a 30 mm diameter disk. The hot catcher operates at a temperature between 1800-2000 K. The delivery time of nuclides to the ECR ion source is < 1.8 s.

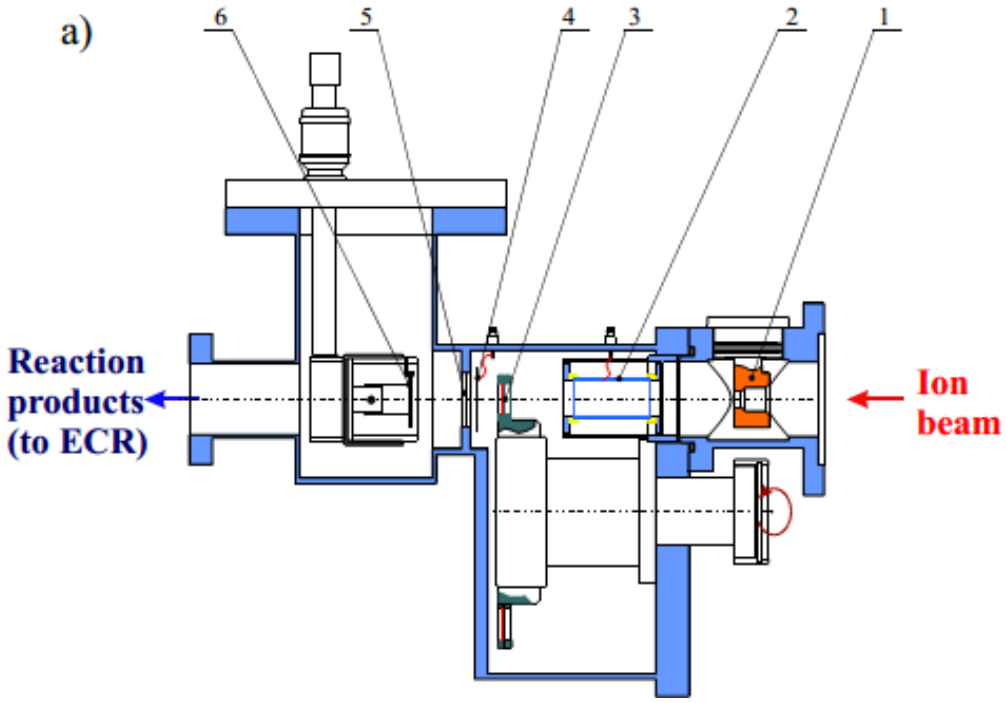

Fig. 2. Target assembly with the hot catcher: (1) diaphragm, (2) pick-up sensor, (3) target on the wheel, (4) electron emission beam monitor, (5) separating foil, (6) hot catcher [2].

Ion source

The ion source is operated under ultra-high frequency conditions at about 2.45 GHz. The incoming atoms of nuclear reaction products are ionized to the charge state Q=+1 and accelerated up to 38 keV by a three-electrode electrostatic lens. The ion beam formed is separated by the magneto-optical mass-to-charge ratio analyser after. Obtained for noble gases, the ionization efficiency reaches 90 % [3].

Detection and data acquisition

A well-type silicon detector is installed in the focal plane of the mass spectrometer to detect decays of nuclear reaction products. The plane of the frontal detector part is oriented along the normal to the beam direction. The diagram of the detector with the key dimensions marked in it is shown in Fig. 3. The frontal detector part covers a 240 ×35 mm^2 area of the focal plane and consists of 192

strips with a pitch of 1.25 mm [1]. Four side detectors are installed around the frontal detector part to increase the geometrical efficiency of detection of reaction product decays. Each of the top and bottom planes is divided into 64 strips, and each of the left and right planes is divided into 16 strips. All detector sections are 300 μm thick, and the thickness of the dead layer at the entrance does not exceed 50 nm. The detector assembly in the focal plane is mounted into a single metal frame. The standard operating bias of the detectors is –40 V, and their energy resolution for α particles from a ^{226}Ra source is ~30 keV [1]. The described geometry of the detector assembly makes it possible to detect no less than 90% α particles emitted in a single nuclear decay at the center of the detector's frontal part [4]. This type of detector can detect alpha particles and fragments, which is suitable for neutron-deficient alpha active nuclei.

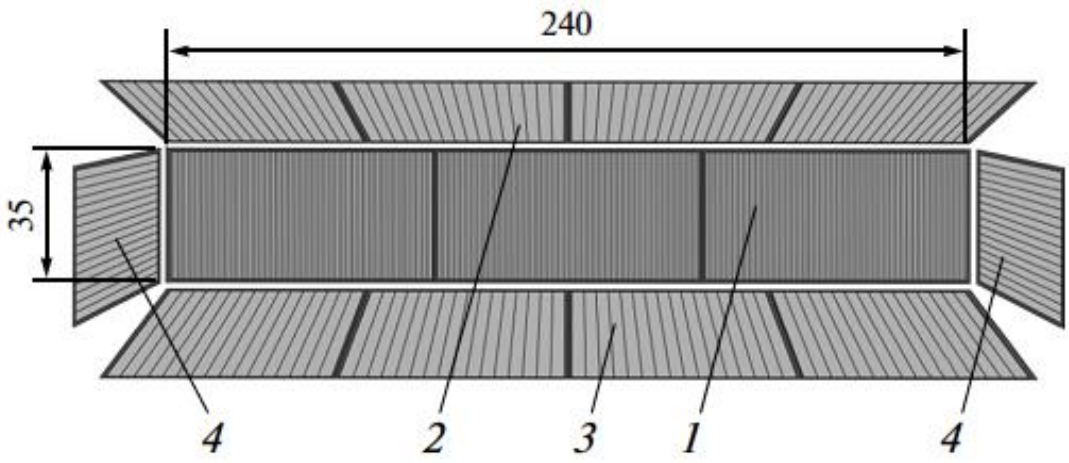

Fig. 3. Silicon detector of the focal plane: (1) frontal part (192 strips), (2) top part (64 strips), (3) bottom part (64 strips), and (4) side parts (16 strips in each) [1].

For the neutron-rich nuclei, which decays mainly by beta minus mode the TIMEPIX pixel detector is used and could be located inside chamber except one of the strip detector crystal. It represents an all-in one box with full sensitive area of 14*14 mm^2 consisting of 256*256 square pixels of pitch size 55 μm and a silicon sensor of 300 μm thickness. This one could detect all types of radiation: α-,β-,γ-radiation, muons, kaons, pions and other charged particles, decay fragments, X-rays in a wide dynamic range and also could be used as a tracking two-dimensional detector.

Signals from the silicon strips were recorded via independent spectrometric channels. The signals came first to the inputs of 16-channel charge-sensitive

preamplifiers located outside of the vacuum chamber. Then it went from the preamplifier outputs to the inputs of 8-channel driver amplifiers with a built-in multiplexer. After amplification and multiplexing, three outputs from the multiplexer were used: alpha, fragment and digital channels. Alpha and fragment signal outputs are the same signals as the source but with different level of amplification. These outputs were connected to the XIA 16-channel high-speed digitizers. The information from the digitizers was read and stored by the NI PXI controller – PXI-8119 [2].

Results and discussion

Three nuclear reactions were studied, obtaining the α energy spectrum of each resulting isotope. A decay and spectrometric analysis of these spectra was made with the help of a nuclide chart, allowing the identification of each nuclear species. Using these energy data, it was able to make an energy calibration of the multi-strip detector and the plot of the energy-position distribution of the different nuclides is shown, improving their identification.

$$^{40}Ar + {}^{148}Sm \rightarrow {}^{188-xn}Hg + xn$$

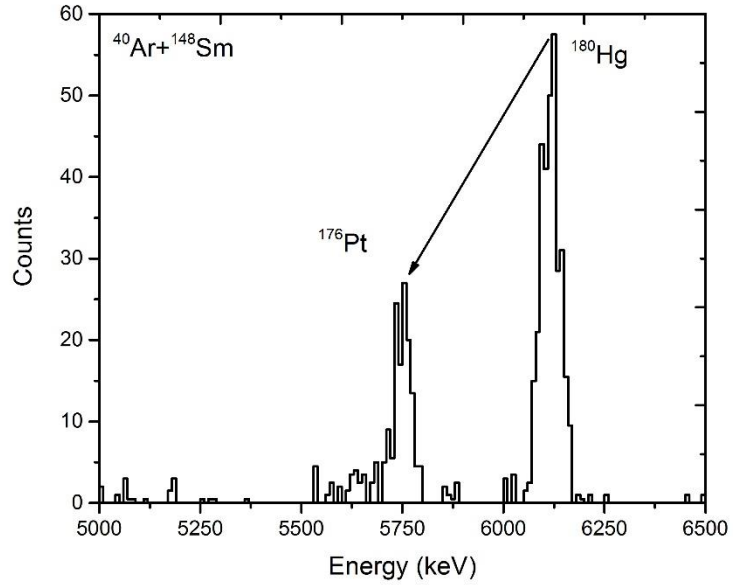

Fig. 4. Energy spectrum of α particles for ^{180}Hg decay. It can be seen the α decay of its daughter nucleus ^{176}Pt.

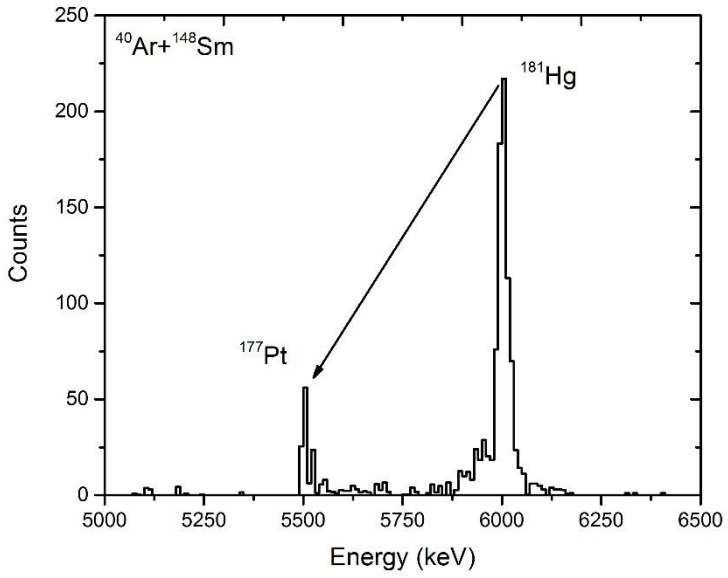

Fig. 5. Energy spectrum of α particles for ^{181}Hg decay. It can be seen the α decay of its daughter nucleus ^{177}Pt.

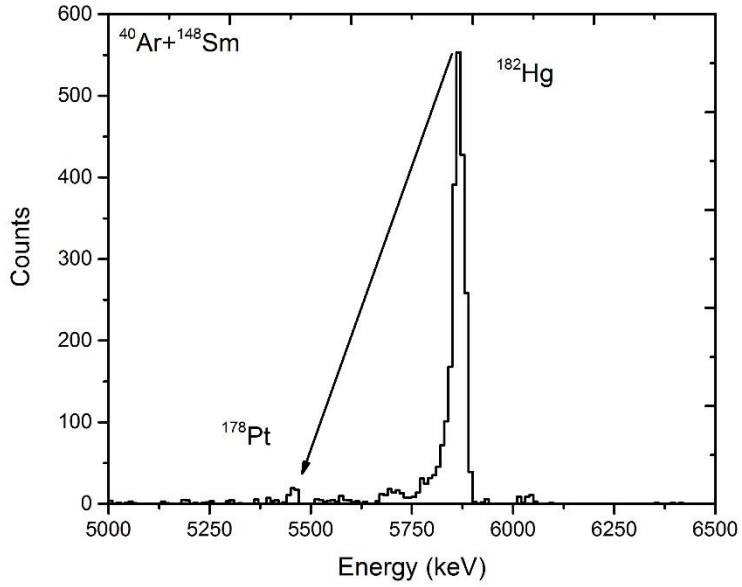

Fig. 6. Energy spectrum of α particles for ^{182}Hg decay. It can be seen the α decay of its daughter nucleus ^{178}Pt.

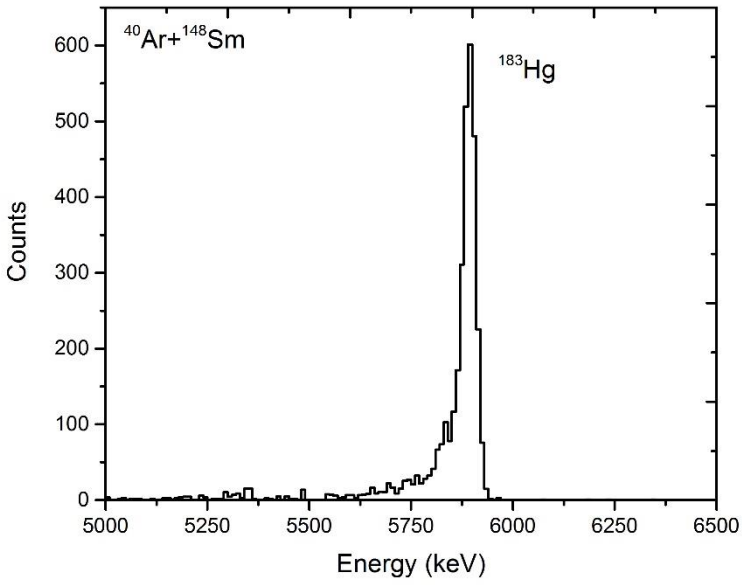

Fig. 7. Energy spectrum of α particles for ^{183}Hg decay.

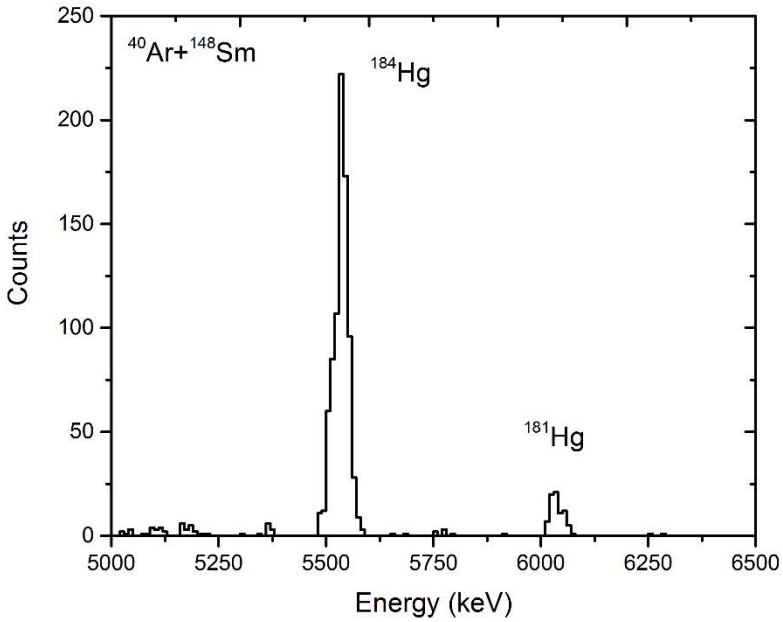

Fig. 8. Energy spectrum of α particles for ^{184}Hg decay. It can be seen also, the α decay of ^{181}Hg.

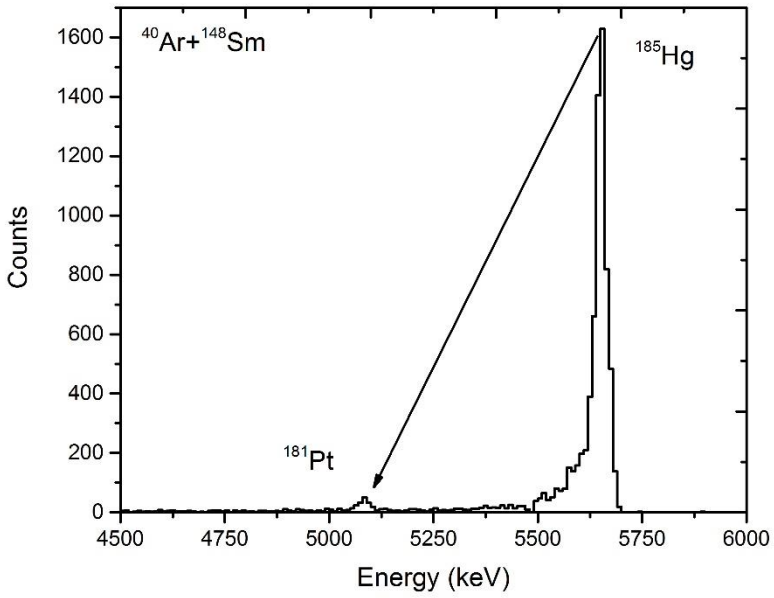

Fig. 9. Energy spectrum of α particles for ^{185}Hg decay. It can be seen the α decay of its daughter nucleus ^{181}Pt.

As can be seen from Figures 4-9, the alpha decay of each Hg isotope is clearly identified as the more intense peak. In addition, for some spectra it is visible the alpha peak of the platinum daughter nucleus, except for Figures 7 and 8, where

it is not visible. It is noticeable in the ^{184}Hg spectrum the presence of what we identified as the decay of ^{181}Hg, possibly due to residues from the previous run.

In Figure 10 it is shown the α decay energy vs. the strip number in the frontal part of the silicon detector located in the focal plane. It is evident the good resolution of the magnetic system and the detector, separating the different isotopes both in mass and in energy.

In Table 1 are presented the fitted α energy from the Hg spectra, together with its corresponding literature value and their relative deviation; most of which are around 2%.

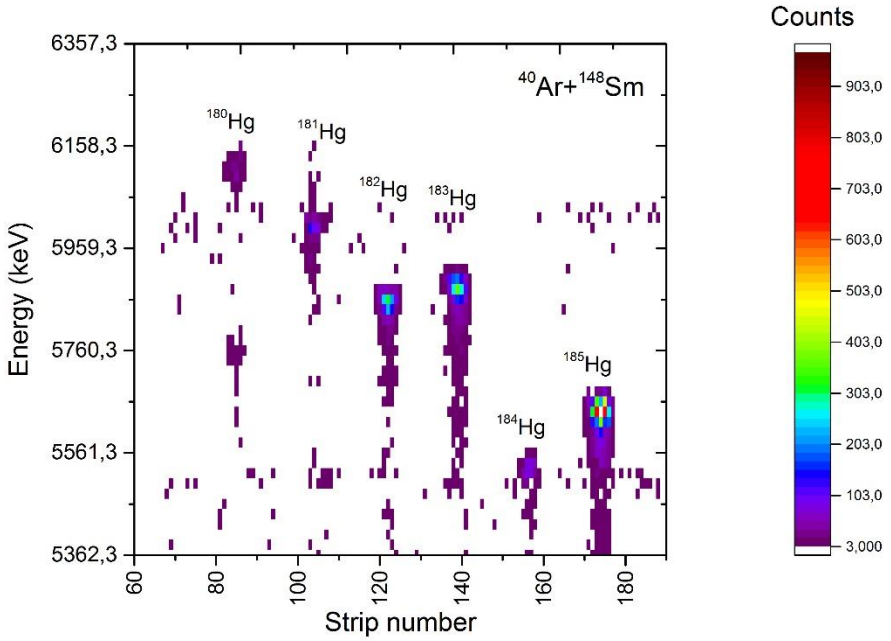

Fig. 10. Two-dimensional energy-position distribution for Hg isotopes.

Table 1. Measured (E_α) and literature ($E_{\alpha,l}$) [5] values of the alpha lines for the identified isotopes. The relative deviation from the literature value is understood as $(E_{\alpha,l} - E_\alpha)/E_{\alpha,l}$

Hg Isotopes	E_α (keV)	$E_{\alpha,l}$ (keV)	Deviation (%)	Pt Isotopes	E_α (keV)	$E_{\alpha,l}$ (keV)	Deviation (%)
^{180}Hg	6111	6258	2,3	^{176}Pt	5745	5885	2,4
^{181}Hg	5998	6284	4,6	^{177}Pt	5497	5643	2,6
^{182}Hg	5861	5996	2,2	^{178}Pt	5452	5573	2,2
^{183}Hg	5888	6039	2,5	^{179}Pt	-	5412	-
^{184}Hg	5532	5660	2,3	^{180}Pt	-	5276	-
^{185}Hg	5646	5773	2,2	^{181}Pt	5080	5150	1,4

$$^{40}Ar + {}^{166}Er \rightarrow {}^{206-xn}Rn + xn$$

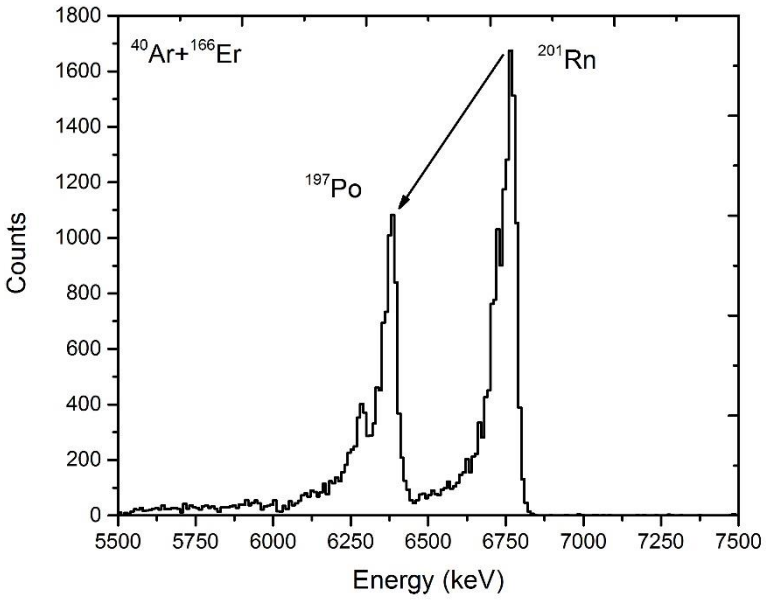

Fig. 11. Energy spectrum of the alpha decay of ^{201}Rn and its daughter nucleus ^{197}Po.

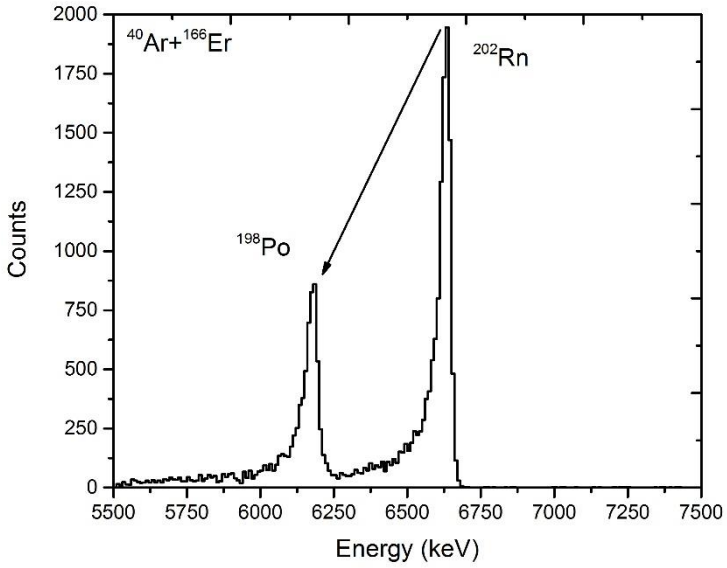

Fig. 12. Energy spectrum of the alpha decay of ^{202}Rn and its daughter nucleus ^{198}Po.

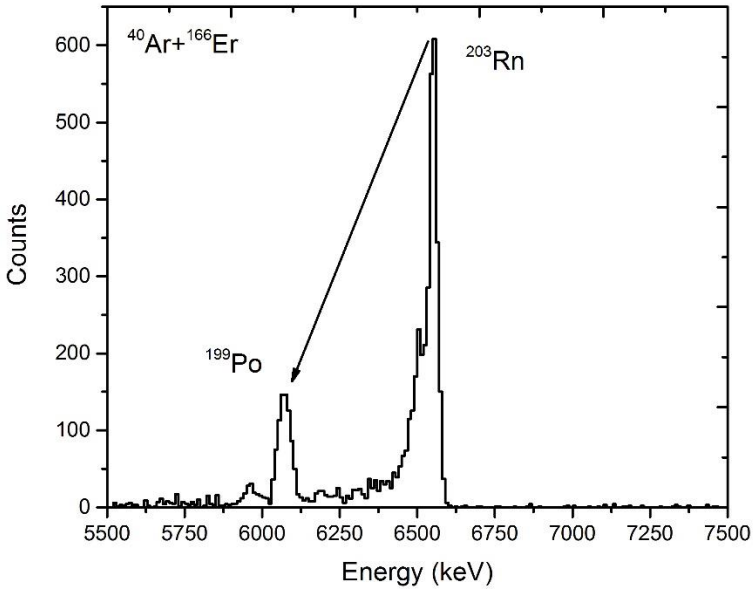

Fig. 13. Energy spectrum of the alpha decay of ^{203}Rn and its daughter nucleus ^{199}Po.

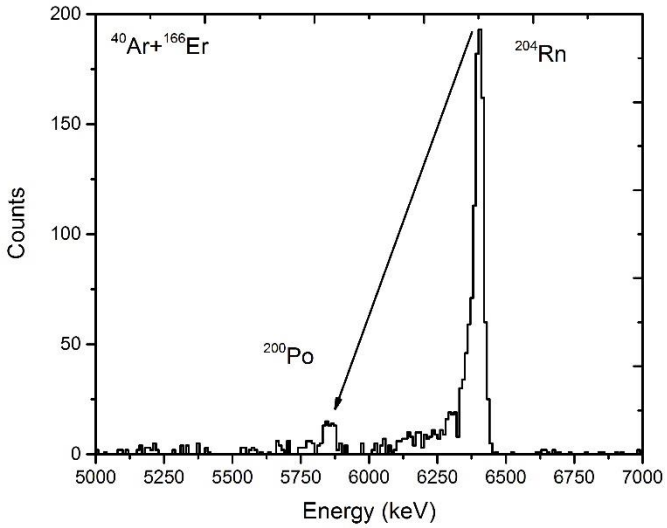

Fig. 14. Energy spectrum of the alpha decay of ^{204}Rn and its daughter nucleus ^{200}Po.

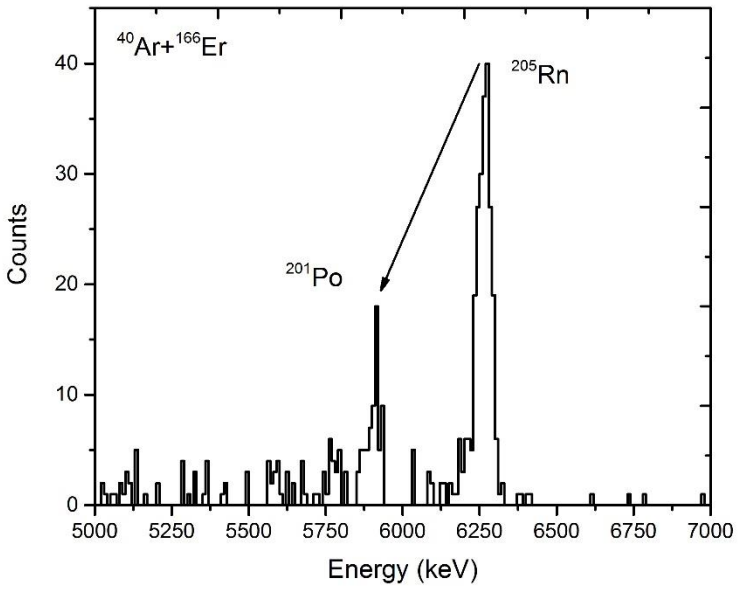

Fig. 15. Energy spectrum of the alpha decay of ^{205}Rn and its daughter nucleus ^{201}Po.

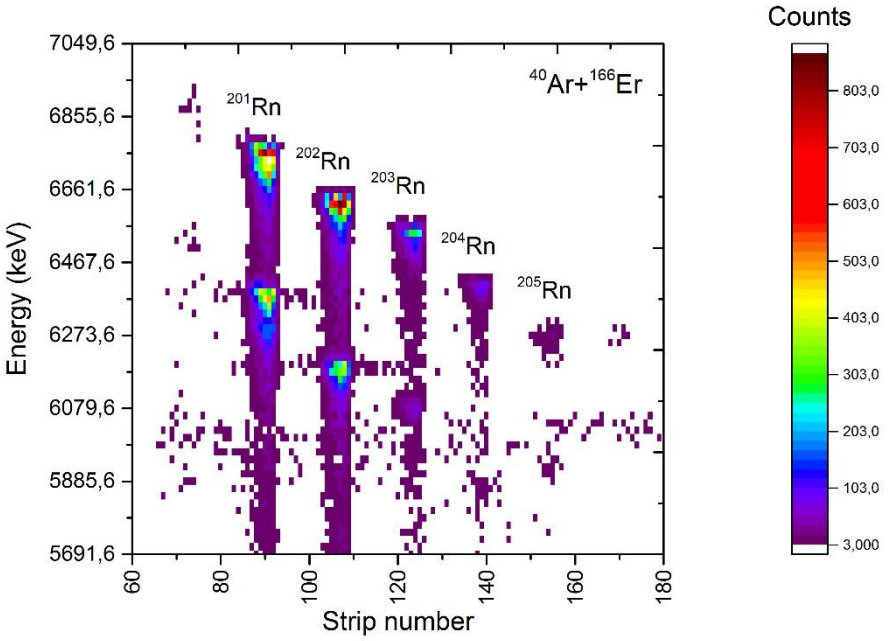

Fig. 16. Energy vs. strip number plot for Rn isotopes.

From Figures 11-15, the α decay peaks of the different Rn isotopes and their Po daughter nuclides are quite evident. Figure 16 shows the α energy-position distribution of the Rn isotopes, again with a very good separation of each nuclear species in both dimensions. In Table 2, it is shown the comparison between the

decay energies measured in this experiment with the literature alpha energies, with an acceptable relative deviation near 2%.

Table 2. Measured (E_α) and literature ($E_{\alpha,l}$) [5] values of the alpha lines for the identified isotopes. The relative deviation from the literature value is understood as $(E_{\alpha,l} - E_\alpha)/E_{\alpha,l}$

Rn Isotopes	E_α (keV)	$E_{\alpha,l}$ (keV)	Deviation (%)	Po Isotopes	E_α (keV)	$E_{\alpha,l}$ (keV)	Deviation (%)
^{201}Rn	6747	6861	1,7	^{197}Po	6368	6411	0,7
^{202}Rn	6623	6774	2,2	^{198}Po	6168	6310	2,3
^{203}Rn	6544	6630	1,3	^{199}Po	6067	6074	0,1
^{204}Rn	6395	6547	2,3	^{200}Po	5848	5982	2,2
^{205}Rn	6261	6386	2,0	^{201}Po	5903	5799	-1,8

$^{48}Ca + {}^{242}Pu$

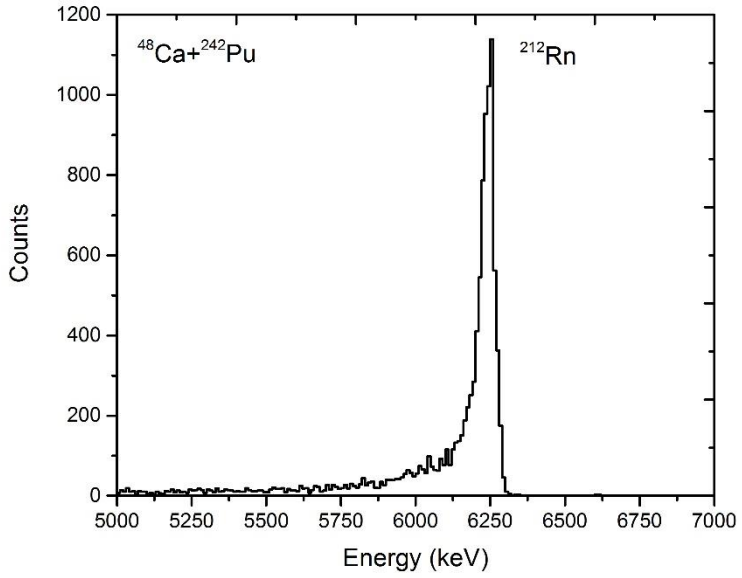

Fig. 17. Energy spectrum of ^{212}Rn.

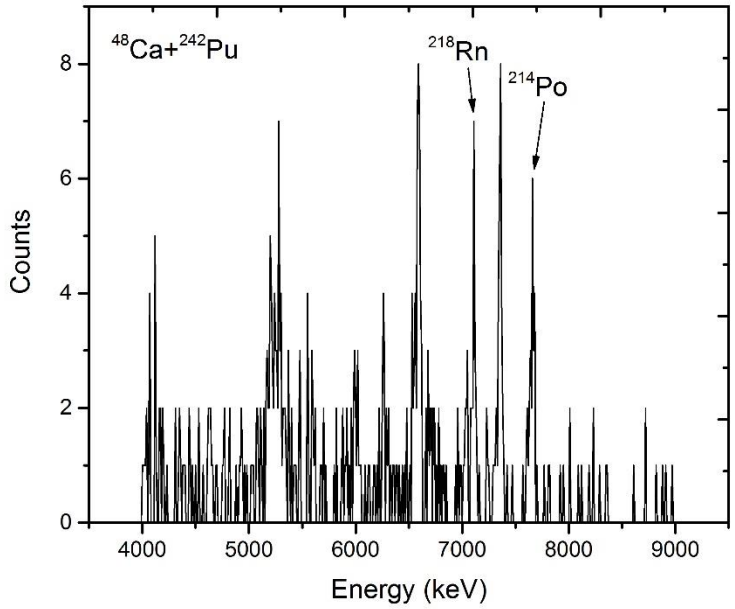

Fig. 18. Energy spectrum of the alpha decay chain $^{218}Rn \rightarrow ^{214}Po \rightarrow ^{210}Pb$.

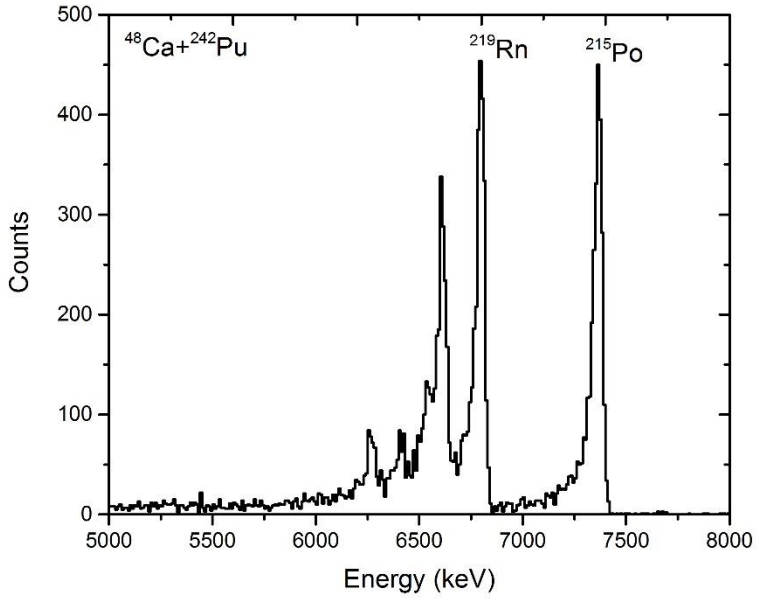

Fig. 19. Energy spectrum of the alpha decay chain $^{219}Rn \rightarrow ^{215}Po \rightarrow ^{211}Pb$.

At Figure 17, only the alpha decay peak of ^{212}Rn appears in the spectrum, unlike at Figure 18, where, among many other peaks it can be seen the alpha decay chain $^{218}Rn \rightarrow ^{214}Po \rightarrow ^{210}Pb$. It is noticeable also, the poor recording statistic of this last spectrum, due to the small lifetime of 35 ms for ^{218}Rn in comparison with the

solid ISOL method response speed, provoking that much of the isotopes were lost inside the catcher. That is the reason why this nuclide is so hard to see on the energy vs. position graph at Figure 20. It can be seen also the alpha lines for ^{219}Rn and its daughter nucleus ^{215}Po along with several other unidentified decay peaks.

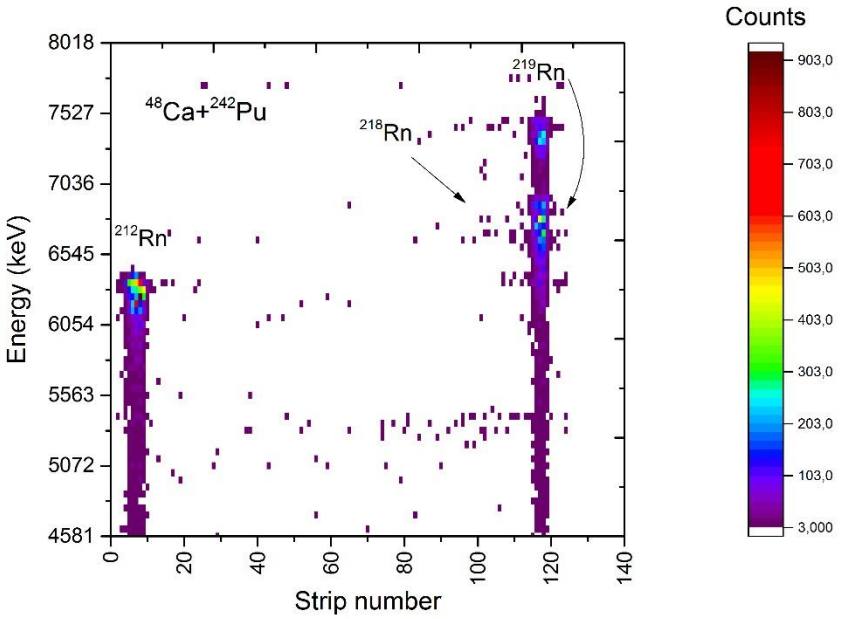

Fig. 20. Energy vs strip number plot for Rn isotopes.

Table 3. Measured (E_α) and literature ($E_{\alpha,l}$) [5] values of the alpha lines for the identified isotopes. The relative deviation from the literature value is understood as $(E_{\alpha,l} - E_\alpha)/E_{\alpha,l}$

Rn Isotopes	E_α (keV)	$E_{\alpha,l}$ (keV)	Deviation (%)	Po Isotopes	E_α (keV)	$E_{\alpha,l}$ (keV)	Deviation (%)
^{212}Rn	6250	6385	2,1	^{208}Po	-	5216	-
^{218}Rn	7110	7262	2,1	^{214}Po	7660	7834	2,2
^{219}Rn	6790	6946	2,2	^{215}Po	7360	7526	2,2

Conclusion

The complete fusion reactions ^{40}Ar+^{148}Sm, ^{40}Ar+^{166}Er and the multinucleon transfer reaction ^{48}Ca+^{242}Pu with their products were analysed with the MASHA facility, previously described. It was shown the alpha decay spectra of each reaction product, identifying them by their decay energy and chain. Through the fitting analysis to the spectra it was able to determine the α energies of the decays, and comparison with its corresponding literature values proved the

correct response of the silicon detector with a relative deviation from the real values, for the majority of nuclides, of no more than 3%. Finally, a two-dimensional matrix of α energy vs. strip number position for all reactions was made, showing the very good separation capability in mass and energy of the multi-strip detector. Direct mass determination of these nuclides could be a plausible task to do with MASHA in the future.

Acknowledgements

I would like to thank my supervisor Mr. Viacheslav Vedeneev for grant me the honour of working with him and for his accurate guidance through this research project. I also wish to thank the INTEREST Program at JINR for giving me the opportunity to participate in this wonderful experience.

References

[1] Rodin, A., Belozerov, A. V., Vanin, D. V. & et. al. MASHA Separator on the Heavy Ion Beam for Determining Masses and Nuclear Physical Properties of Isotopes of Heavy and Superheavy Elements. Instruments and Experimental Techniques **57**, 386-393 (2014).

[2] Vedeneev, V. Y., Rodin, A., Krupa, L. & et. al. The current status of the MASHA setup. Hyperfine Interactions **238:19** (2017).

[3] Efremov, A., Bekhterev, V., Bogomolov, S. & et al. Nucl. Inst. Methods B **2**(04), 368–371 (2003).

[4] Rodin, A. M., Belozerov, A. & et. al. Separation efficiency of the MASHA facility for short-lived mercury isotopes. Hyperfine Interactions **227**, 209-221 (2014).

[5] LiveChart of Nuclides-Advanced version. IAEA. www-nds.iaea.org.